# Multiorder rotational Raman transitions in molecular alignment and orientation

Shuwu Xu [1,*] Zhenzhong Lian [2,*] Qian-Qian Hong [2] Lingxiao Wang [1] Huajie Chen,[1]
Yunxia Huang,[1,†] and Chuan-Cun Shu [2,‡]

[1]*School of Physics and Technology, Nantong University, Nantong 226019, China*
[2]*Hunan Key Laboratory of Nanophotonics and Devices, Hunan Key Laboratory of Super-Microstructure and Ultrafast Process,
School of Physics, Central South University, Changsha 410083, China*

Nonresonant two-photon Raman transitions with $\Delta J = \pm 2$ selection rules induce molecular alignment by altering the rotational quantum number $J$, whereas three-photon Raman transitions with $\Delta J = \pm 1$ cause molecular orientation. Here, we perform a combined numerical and theoretical investigation to explore how these Raman transitions depend on laser intensity and to discern multiorder Raman transitions in laser-induced alignment and orientation going beyond two- and three-photon processes. Our results demonstrate the presence of higher-order transitions in molecular alignment and shed light on how alignment affects subsequent three-photon rotational Raman transitions as revealed by the alignment and orientation spectra and the Dyson series expansion of the unitary operator. As the laser pulse strength increases, multiorder transitions become directly observable, which can be utilized to enhance the alignment and orientation of molecules through the excitation of multiple rotational states.

## I. INTRODUCTION

With advancements in ultrafast laser technology, the creation of molecular alignment and orientation through ultrashort laser pulses has gained significant prominence, showcasing promising applications in physics, chemistry, and quantum information techniques [1–3]. These applications include enhancing high-order harmonic generation [4–6], studying the dependence of ionization rates in molecules [7–10], investigating rotational echoes [6,11–13], controlling molecular rotation [14–18], and imaging molecular orbitals [19,20], among others [21–24]. Molecular alignment involves ordering the molecular axis relative to a fixed spatial axis, while orientation specifies a preferred direction. Intense laser pulses have proven highly effective for achieving molecular alignment [25–29]. Two commonly used approaches to induce molecular orientation are using intense nonresonant interactions of optical pulses with the polarizability and hyperpolarizability [30–35] or using resonant interactions of terahertz pulses with the permanent dipole moment [36–44], leading to field-free molecular alignment and orientation.

The advantage of nonresonant excitation schemes, where laser frequencies are set far from vibrational and electronic transition frequencies, lies in their ability to achieve field-free molecular alignment and orientation without relying on permanent dipole interaction. The torque exerted by the laser field on molecular polarizability induces changes in rotational states of $\Delta J = \pm 2$ resulting in alignment, while further changes in hyperpolarizability with $\Delta J = \pm 1$ lead to orienta-tion. In terms of the underlying physical mechanics, one-order nonresonant two-photon Raman transitions occur for generating alignment, whereas three-photon Raman transitions are induced for generating molecular orientation [31,34,45–50]. Recently, we conducted an experimental study, supported by theoretical analysis and numerical simulations, to elucidate the underlying process behind the alignment revivals induced by a pair of nonresonant femtosecond laser pulses on air molecules at room temperature [51]. Our time-resolved two-dimensional alignment measurements revealed that one-order two-photon nonresonant Raman transitions from initial states of mixed molecules play a dominant role, exhibiting a signature of weak-field-induced alignment phenomena. When molecules are exposed to intense ultrashort pulses, understanding the underlying transition mechanism becomes complex, yet it is essential for developing quantum control strategies to manipulate alignment and orientation. In this paper, we show how multiorder Raman transitions occur in nonresonant laser-induced molecular alignment and orientation. This effect is particularly significant in molecular orientation under relatively high intensities. We explain how these Raman transitions depend on laser intensity and initial states by using Fourier transforms of the time-dependent molecular alignment and orientation factors and the Dyson series expansion of the unitary operator. This paper will enhance our understanding of nonresonant Raman transitions in laser-induced molecular alignment and orientation.

The paper is organized as follows: Sec. II outlines the theoretical methods for describing nonresonant laser-induced alignment and orientation of molecules at room temperature. In Sec. III, numerical simulations and discussions are conducted to analyze multiorder Raman transitions in alignment and orientation. Finally, our findings are summarized in Sec. IV.

---

*These authors contributed equally to this work.
†Contact author: hyx@ntu.edu.cn
‡Contact author: cc.shu@csu.edu.cn

## II. THEORETICAL METHODS

### A. Numerical model

We begin by considering polar molecules initially in the ground vibrational and electronic state. In the absence of vibrational excitation, the field-free Hamiltonian $\hat{H}_0$ of the molecule within the rigid-rotor approximation can be expressed as

$$\hat{H}_0 = B\hat{J}^2, \tag{1}$$

where $B$ represents the rotational constant of the molecular ground state, and $\hat{J}$ denotes its angular momentum operator. For the case of laser-induced alignment, we employ a linearly polarized single-color pulse

$$\mathcal{E}(t) = \mathcal{E}_0 f(t) \cos(\omega_0 t), \tag{2}$$

while for laser-induced orientation, a pair of two-color pulses is utilized:

$$\mathcal{E}(t) = \mathcal{E}_0 f(t)[\cos(\omega_0 t) + \cos(2\omega_0 t)], \tag{3}$$

where $f(t)$ represents the pulse envelope with a Gaussian profile given by $f(t) = \exp[(-2\ln 2)t^2/\tau_0^2]$. $\mathcal{E}_0$ denotes the electric-field strength, $\omega_0$ stands for the central frequency, and $\tau_0$ represents the duration of the pulse.

For nonresonant excitation, where the laser field's center frequency is significantly different from the rotational frequencies of the molecule, resonant excitation via the permanent dipole moment can be neglected. The interaction Hamiltonian is given by

$$\hat{H}_c(t) = -\tfrac{1}{2}\mathcal{E}^2(t)[(\alpha_\parallel - \alpha_\perp)\cos^2\theta + \alpha_\perp] \\ -\tfrac{1}{6}\mathcal{E}^3(t)[(\beta_\parallel - 3\beta_\perp)\cos^3\theta + 3\beta_\perp\cos\theta], \tag{4}$$

where $\theta$ represents the angle between the field's polarization direction and the molecular axis. Here, $\alpha_\parallel$ and $\alpha_\perp$ denote the polarizability components, while $\beta_\parallel$ and $\beta_\perp$ correspond to the hyperpolarizability components, aligned parallel and perpendicular to the molecular axis, respectively.

For excitation processes that are linearly polarized, the quantum number $M$, which denotes the projection of angular momentum along the polarization axis, remains constant. The time-dependent wave packet of the molecules initially in the state $J_0 M_0$ can be written as

$$\psi_{J_0 M_0}(\theta, \phi, t) = \sum_{J' \geqslant |M_0|} c_{J' M_0}(t) \exp(-i\omega_{J'} t/\hbar) Y_{J' M_0}(\theta, \phi), \tag{5}$$

where the initial state is given by $Y_{J_0 M_0}(\theta, \phi) = \langle \theta, \phi | J_0 M_0 \rangle$, and $c_{J' M_0}(t)$ denotes the expansion coefficient of the state $|J' M_0\rangle$. Since the quantum number $|M| \leqslant J$, only states with $J' \geqslant |M_0|$ contribute to the summation. The functions $Y_{J' M_0}(\theta, \phi)$ represent spherical harmonics that comply with the relation $\hat{H}_0 Y_{J' M_0}(\theta, \phi) = E_{J'} Y_{J' M_0}(\theta, \phi)$, where $\omega_{J'}$ denotes the eigenfrequency defined by $\omega_{J'} = BJ'(J'+1)$. We

can numerically solve the corresponding time-dependent Schrödinger equation with Hamiltonian $\hat{H}(t) = \hat{H}_0 + \hat{H}_c(t)$ to obtain the wave packet $\psi_{J_0 M_0}(\theta, \phi, t)$.

In the context of molecular alignment and orientation, the degrees to which these phenomena occur are quantified by the expectation values $\langle \cos^2 \theta \rangle$ and $\langle \cos \theta \rangle$, respectively. When considering a molecular ensemble at thermal equilibrium, these degrees need to be averaged over a Boltzmann distribution. The degree of alignment can be represented mathematically as

$$\langle \cos^2 \theta \rangle = \sum_{J_0} \frac{g_{J_0} \exp[-BJ_0(J_0+1)/k_B T]}{Q} \\ \times \sum_{M_0 = -J_0}^{J_0} \langle \psi_{J_0 M_0} | \cos^2 \theta | \psi_{J_0 M_0} \rangle, \tag{6}$$

while the degree of orientation can be given by

$$\langle \cos \theta \rangle = \sum_{J_0} \frac{g_{J_0} \exp[-BJ_0(J_0+1)/k_B T]}{Q} \\ \times \sum_{M_0 = -J_0}^{J_0} \langle \psi_{J_0 M_0} | \cos \theta | \psi_{J_0 M_0} \rangle, \tag{7}$$

where $g_{J_0}$ is the spin degeneracy factor, $k_B$ is the Boltzmann constant, $T$ is the temperature, and $Q = \sum_{J_0=0}^{\infty}(2J_0+1)e^{-BJ_0(J_0+1)/k_B T}$ is the rotational partition function. These expressions allow us to understand how thermal motion affects the molecular alignment and orientation induced by applied pulses, integrating statistical thermodynamics with quantum mechanics to describe these phenomena comprehensively.

### B. Analytical description

To explain the underlying excitation mechanism, we calculate the expansion coefficient $c_{J' M_0}$ in Eq. (5) by $c_{J' M_0}(t) = \langle J' M_0 | \hat{U}(t, t_0) | J_0 M_0 \rangle$, where the unitary evolution operator in the interaction picture reads

$$\hat{U}(t, t_0) = \hat{U}(t_0, t_0) - i \int_{t_0}^{t} dt' \hat{V}_I(t') U(t', t_0), \quad \hat{U}(t_0, t_0) = \mathcal{I}, \tag{8}$$

with $\hat{V}_I(t) = \exp(i\hat{H}_0 t)[\hat{H}_c(t)] \exp(-i\hat{H}_0 t)$ by defining the field-free Hamiltonian $\hat{H}_0$,

$$\hat{H}_0 = \sum_{J=|M_0|} BJ(J+1)|JM_0\rangle\langle JM_0|, \tag{9}$$

and

$$\hat{H}_c(t) = -\tfrac{1}{2}\mu_\alpha \mathcal{E}^2(t) - \tfrac{1}{6}\mu_\beta \mathcal{E}^3(t). \tag{10}$$

The off-diagonal matrix elements of $\mu_\alpha$ in Eq. (10) with the two-photon selection rules $\Delta J = \pm 2$ can be defined by

$$\mu_\alpha(JM_0, J \pm 2M_0) = \langle JM_0 | [(\alpha_\parallel - \alpha_\perp)\cos^2\theta + \alpha_\perp] | J \pm 2, M_0 \rangle$$

$$= (\alpha_\parallel - \alpha_\perp) \frac{\sqrt{(J \pm 1)^2 - M_0^2}\sqrt{(J+1+1)^2 - M_0^2}}{\sqrt{(2J \pm 1)(2J \pm 3)}\sqrt{[2(J \pm 1) + 1][2(J \pm 1) + 3]}}, \tag{11}$$

whereas the diagonal matrix elements are

$$\mu_\alpha(JM_0, JM_0) = \langle JM_0|[(\alpha_\parallel - \alpha_\perp)\cos^2\theta + \alpha_\perp]|JM_0\rangle$$

$$= (\alpha_\parallel - \alpha_\perp)\frac{4J^3 + 6J^2 - (4J+2)M_0^2 - 1}{(2J-1)(2J+1)(2J+3)} + \alpha_\perp. \tag{12}$$

The off-diagonal matrix elements of $\mu_\beta$ in Eq. (10) with the three-photon selection rule $\Delta J = \pm 1$ can be given by

$$\mu_\beta(JM_0, J+1 M_0) = \langle JM_0|[(\beta_\parallel - 3\beta_\perp)\cos^3\theta + 3\beta_\perp\cos\theta]|J+1, M_0\rangle$$

$$= (\beta_\parallel - 3\beta_\perp)\frac{\sqrt{(J+1)^2 - M_0^2}}{\sqrt{(2J+1)(2J+3)}}\left\{\frac{(J+1)^2 - M_0^2}{(2J+1)(2J+3)} + \frac{(J+2)^2 - M_0^2}{(2J+3)(2J+5)} + \frac{J^2 - M_0^2}{(2J-1)(2J+1)}\right\}$$

$$+ 3\beta_\perp\frac{\sqrt{(J+1)^2 - M_0^2}}{\sqrt{(2J+1)(2J+3)}}, \tag{13}$$

and

$$\mu_\beta(JM_0, J-1 M_0) = \langle JM_0|[(\beta_\parallel - 3\beta_\perp)\cos^3\theta + 3\beta_\perp\cos\theta]|J-1, M_0\rangle$$

$$= (\beta_\parallel - 3\beta_\perp)\frac{\sqrt{J^2 - M_0^2}}{\sqrt{(2J-1)(2J+1)}}\left\{\frac{J^2 - M_0^2}{(2J-1)(2J+1)} + \frac{(J+1)^2 - M_0^2}{(2J+1)(2J+3)} + \frac{(J-1)^2 - M_0^2}{(2J-3)(2J-1)}\right\}$$

$$+ 3\beta_\perp\frac{\sqrt{J^2 - M_0^2}}{\sqrt{(2J-1)(2J+1)}}. \tag{14}$$

To gain insights into the underlying transitions between states, the Dyson series expansion of the unitary operator can be given by [52,53]

$$\hat{U}(t, t_0) = \hat{I} - i\int_{t_0}^t \hat{V}_I(t_1)dt_1 + (-i)^2\int_{t_0}^t \hat{V}_I(t_2)dt_2\int_{t_0}^{t_2}\hat{V}_I(t_1)dt_1 + \cdots. \tag{15}$$

We can analyze that the first-order expansion term via the polarizability interaction results in transitions of $\Delta J = \pm 2$, while the corresponding hyperpolarizability interaction yields $\Delta J = \pm 1$ transitions, which can describe the Raman transitions induced by relatively weak lasers, as illustrated in Fig. 1. For higher laser intensities, higher-order Raman transitions occur from $J_0$ to states $J_0 = \pm 4$, either directly or indirectly via intermediate states $J_0 \pm 2$ [see Fig. 1(a)], influenced by interactions with polarizability. In addition to direct orientation transitions from $J_0$ to $J_0 \pm 1$, there are also indirect orientation transitions from $J_0 \pm 2$, induced by the interaction of two pulses with the polarizability, as shown in Fig. 1(b). By comparing the transition probabilities using the Dyson expansion of the unitary operator in Eq. (15) to different orders $n$ with exact simulations using Eq. (8), we can identify various orders of Raman transitions.

## III. RESULTS AND DISCUSSION

To illustrate, we use the carbon monoxide (CO) molecule as an example, with corresponding molecular parameters [33,54] listed in Table I. The fundamental frequency of the laser pulse is set to $\omega_0 = 12\,500$ cm$^{-1}$, corresponding to a wavelength of 800 nm. Unless specified otherwise, the duration for both single- and two-color laser pulses is $\tau_0 = 100$ fs, and the molecular rotational temperature is $T = 300$ K.

### A. Multiorder rotational Raman transitions in alignment

Figure 2 depicts the time-dependent degrees of alignment induced by a single-color pulse described by Eq. (2) at two different laser intensities of $I_0 = 0.3 \times 10^{13}$ and $3.0 \times 10^{13}$ W/cm$^2$. It clearly shows the periodic revival of alignment, with a revival period of approximately 8.64 ps, consistent with the theoretical value of $\pi/B$, whereas the maximum alignment value revival at the half period is 4.32 ps. Furthermore, the higher intensity laser pulse results in enhanced alignment compared to the lower intensity pulse, although their behaviors in Figs. 2(a) and 2(b) appear similar. Figure 3 shows the Fourier-transform spectra of the revival alignment signals depicted in Fig. 2. The peaks in these spectra correlate with the coherence between adjacent states with $\Delta J = \pm 2$, revealing the presence of Raman transitions at frequency $(4J + 6)B$. To examine how different initial states contribute to the laser-induced alignment, we calculate the Fourier-transform spectra of the time-dependent alignment signal originating from different initial states as well.

At low intensity of $I_0 = 0.3 \times 10^{13}$ W/cm$^2$ in Fig. 3(a), an overall spectrum ranging to approximately $J = 25$ is shown at the top. The spectrum for each initial state reveals that only the adjacent transitions with $\Delta J = \pm 2$ happen under the current pulse intensity. Specifically, for the initial state $J_0 = 0$ depicted, only the transition to the state $J = 2$ occurs, peaking at $6B$. For initial states of $J_0 = 3, 4, 15,$ and 16, the excitation from $J_0$ to $J_0 + 2$ is more prominent than the deexcitation to
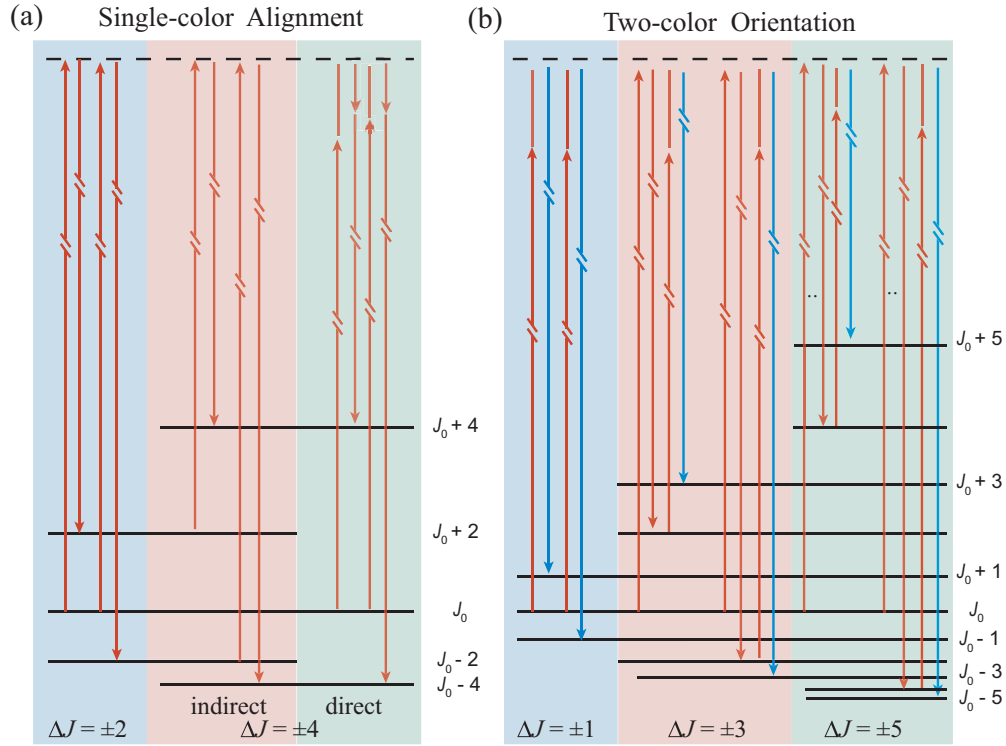
FIG. 1. Schematic illustration of Raman transitions in (a) single-color pulse induced molecular alignment and (b) two-color pulse induced molecular orientation. Different areas from left to right depict the transitions that may happen from initial state $J_0$ as the laser intensity increases. The adjacent states $J_0 \pm 2$ are excited via a two-photon process involving virtual states, indicated by a dashed line.

$J_0 - 2$, which is reversed for the initial state of $J_0 = 10$. This behavior can be explained by comparing the transition dipole moments using Eq. (11) and considering the degeneracy of the initial states $J_0$ that can be deexcited into $J_0 - 2$ and excited into $J_0 + 2$ due to the constraint of $\Delta M = 0$. Furthermore, analytic formulas for the expansion coefficients of the rotational wave packet, based on Eqs. (11)–(14) and a first- or second-order propagator expansion, are more useful, because they are directly related to the peaks in Fig. 3. However, in multiorder Raman excitations, these calculations are challenging due to the involvement of multiple rotational states.

At high laser intensity of $I_0 = 3 \times 10^{13}$ W/cm$^2$, transitions become more complex, leading to transitions to higher rotational states. As shown in Fig. 3(b), more peaks are observed in the spectra originating from different initial states. This highlights the emergence of the multiorder Raman transition as well as its high sensitivity to the initial states, resulting in different excitations and deexcitations. This sensitivity is due to the transition dipole moment and the influence of the excitation pulse bandwidth. Specifically, when the initial state is $J_0 = 0$, further Raman transitions to high rotational states are less likely due to the weak transition dipole moment. However, the prevalence of this phenomenon from higher

rotational states, e.g., $J_0 = 15$ and 16, can be attributed to scenarios where the energy spacing between adjacent states is larger than the excitation pulse bandwidth.

To further understand the rotational Raman transitions under different laser intensities, we use the Dyson series expansions of the unitary operator in Eq. (15) up to the second order to calculate rotational state populations, which are then compared with the exact calculations by Eq. (8). Figures 4(a) and 4(b) show the final populations of rotational states for the
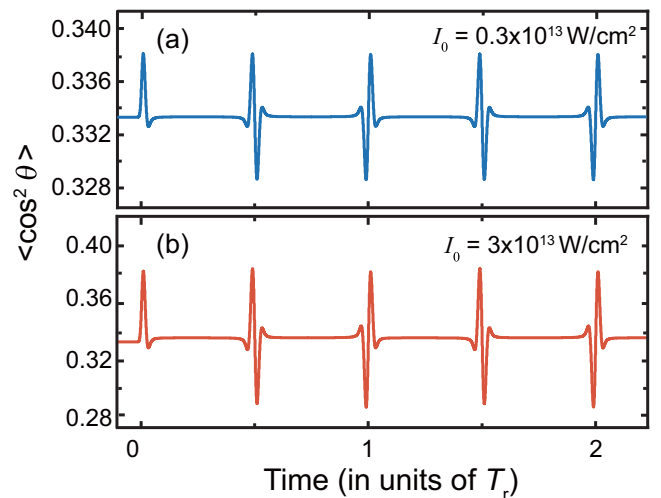


FIG. 2. Time-dependent molecular alignment of CO molecules for laser intensities of (a) $I_0 = 0.3 \times 10^{13}$ W/cm$^2$ and (b) $I_0 = 3 \times 10^{13}$ W/cm$^2$.

TABLE I. Molecular parameters of CO.

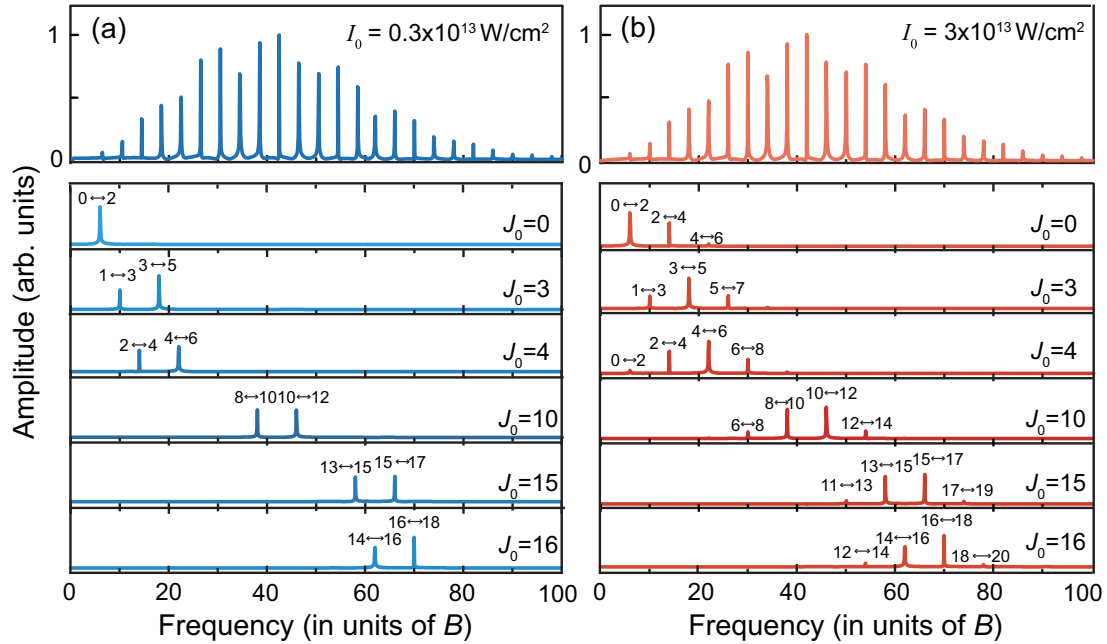| | $B$ (cm$^{-1}$) | $\alpha_\parallel$ (Å$^3$) | $\alpha_\perp$ (Å$^3$) | $\beta_\parallel$ ($\times 10^9$ Å$^5$) | $\beta_\perp$ ($\times 10^8$ Å$^5$) |
|---|---|---|---|---|---|
| CO | 1.928 | 2.294 | 1.77 | 2.748 | 4.994 |

FIG. 3. Fourier transform of the CO molecular alignment signals for (upper row) overall rotational states and (lower row) some of the initial rotational states with the excitation laser intensity of (a) $I_0 = 0.3 \times 10^{13}$ W/cm$^2$ and (b) $I_0 = 3 \times 10^{13}$ W/cm$^2$.

initial state $J_0 = 0$. In Fig. 4(a), we notice that the populations of rotational state $J = 2$ calculated using both the first- and second-order approximations coincide with the exact results very well at the low intensity region. The divergence between the first-order approximation and the exact results appears when the laser intensity approaches $1.0 \times 10^{13}$ W/cm$^2$ while the second-order approximation still applies. This indicates the emergence of multiorder transition that leads to higher rotational states $J = 4$, which can be clearly demonstrated in Fig. 4(b). For the case of the initial state $J_0 = 16$ depicted in Fig. 4(c), both the adjacent states $J = 14$ and 18 are presented. The divergence of the results calculated using first-order Dyson expansion from the exact calculation also appears around $1.0 \times 10^{13}$ W/cm$^2$, leading to the generation of higher states $J = 12$ and 20 shown in Fig. 4(d). The difference between populations originated from the upper and lower transition can also be explained by the transition dipole moments using Eq. (11).

### B. Multiorder rotational Raman transitions in orientation

Figure 5 illustrates the simulations depicting the degrees of orientation induced by two-color pulses as described in Eq. (3) at two different laser intensities of $I_0 = 0.3 \times 10^{13}$ and $3.0 \times 10^{13}$ W/cm$^2$. The orientations display periodic revival of 8.64 ps, and an increase in intensity results in enhanced orientation. As two types of transition depicted in Fig. 1 exist at the same time, the excitation process in orientation becomes much more complex than that of the alignment. To have a clear vision on how the different types of transition contribute to the signal, we also calculate the degrees of orientation with hyperpolarizability alone, i.e., without considering the first term in Eq. (4). As can be seen, when $I_0 = 0.3 \times 10^{13}$ W/cm$^2$, the degrees of orientation obtained from two methods overlap almost without evident difference. This is due to the fact

that the coupling between the rotational states with $\Delta J = \pm 1$ is induced by the hyperpolarizability at lower intensities. The influence of the polarizability to the signal via changing the population of higher states is very limited. However, when the intensity increases, the difference becomes evident as shown in Fig. 5(b). This reveals that the transition $\Delta J = \pm 2$ induced via polarizability starts to cause notable change in the signal $\langle \cos \theta \rangle$. The alteration is mainly due to the fact that the transition of $\Delta J = \pm 1$ induced by hyperpolarizability begins to couple with the transitions induced by the polarizability with $\Delta J = \pm 2$ as the intensity increases, i.e., multiorder Raman transition as depicted in Fig. 1(b) occurs.

Figure 6 depicts the Fourier spectra obtained from the orientation signal calculated with and without considering the polarizability at two different laser intensities. In contrast to the alignment spectra depicted in Fig. 3, both the positions and intervals of each spectral peak are reduced, indicating a coupling between rotational states with $\Delta J = \pm 1$ caused by the nonresonant three-photon Raman transition. The spectra of various initial states have also been considered. In Fig. 6(a), we notice that the overall spectra for both situations display identical outlines when the intensity is low. For the initial state with $J_0 = 0$ when considering both the polarizability and hyperpolarizability, there is a prominent peak at $2B$ corresponding to the transition from 0 to 1, and another peak at the $4B$ position indicating coherence between $J = 1$ and 2. The higher excited rotational state $J = 2$ is induced by polarizability in Fig. 1(b) rather than a higher-order transition via three-photon Raman transition, since it cannot be observed in the spectrum underneath where the polarizability is excluded. Similarly, for higher initial states $J_0 = 10$ and 16, the spectra without considering the polarizability have only two peaks corresponding to the couplings between $J_0$ and $J_0 \pm 1$. The small peaks relating to the coupling between higher rotational states come from the simultaneous presence of two types
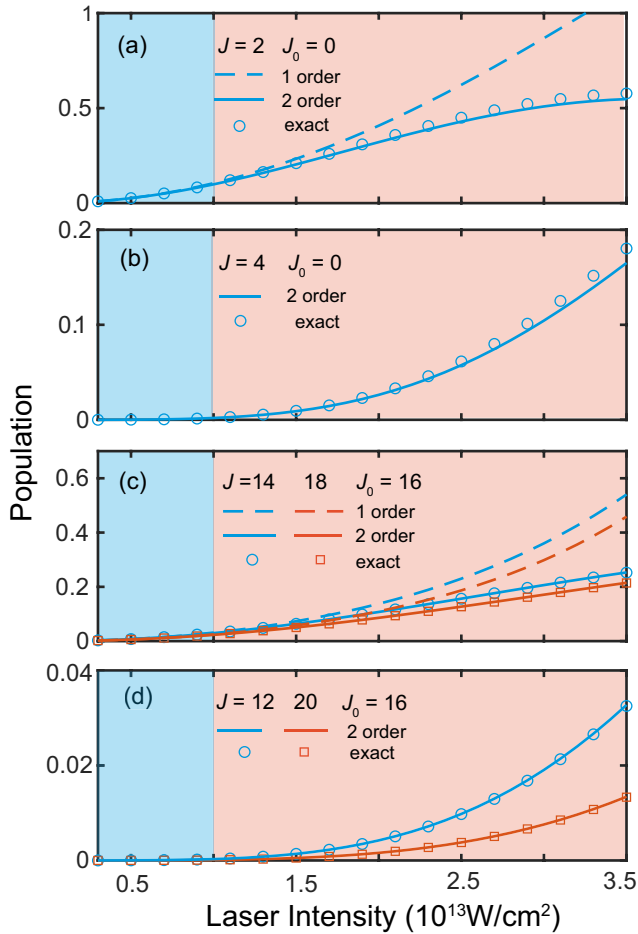
FIG. 4. The dependence of the population for different rotational states on the laser intensity. The population of (a) $J = 2$ and (b) $J = 4$ from the initial states $J_0 = 0$ is calculated using different methods: exact numerical, and the first- and the second-order Dyson series expansion of the unitary operator. (c, d) The population of (c) $J = 14$ and 18 (d) $J = 12$ and 20 from the initial states $J_0 = 16$ calculated with different methods.



FIG. 5. Time-dependent molecular orientation of CO molecules for laser intensities of (a) $I_0 = 0.3 \times 10^{13}$ W/cm$^2$ and (b) $I_0 = 3 \times 10^{13}$ W/cm$^2$. The dashed and solid lines correspond to the results obtained by considering both the polarizability and hyperpolarizability and only considering the hyperpolarizability in calculation, respectively.

of Raman transition. Note that the coherences between the higher states are too small to affect the overall $\langle \cos \theta \rangle$ signal in Fig. 5(a) and the overall Fourier-transform spectrum.

The spectral peaks depicted in Fig. 6(b) demonstrate increased complexity as $I_0$ increases. For the overall spectra shown at the top, when both polarizability and hyperpolarizability are taken into account, the higher-energy peaks become more prominent. For a given initial state $J_0 = 0$, eight distinct peaks are observed, with the fifth peak exhibiting the greatest intensity. However, considering only the hyperpolarizability yields a singular peak, much like the result obtained at low laser intensity on the left. This indicates that hyperpolarizability alone still cannot lead to higher $J$ rotational states with the current laser intensity. The presence of multiple peaks arises from the process involving transitions to higher rotational states through polarizability-induced excitations, followed by transitions between adjacent $J \pm 1$ states via hyperpolarizability as shown in Fig. 1(b), or vice versa. This suggests the existence of multiorder Raman transitions between different types of transitions. Similar results are obtained when the ini-
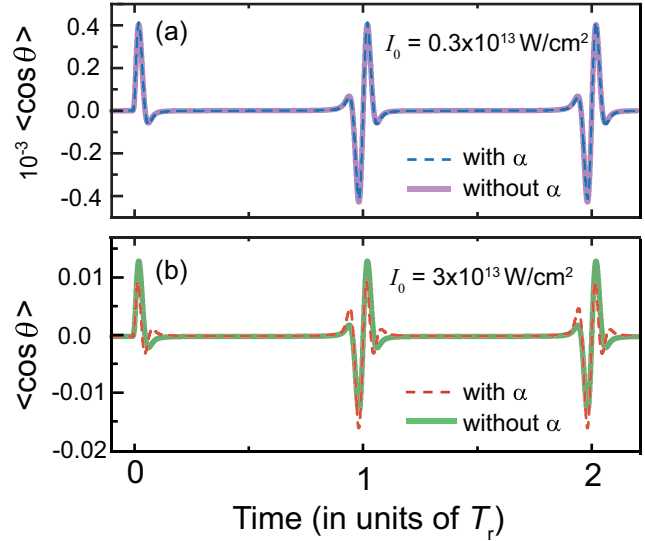
tial states $J_0 = 10$ and 16 are selected. The spectrum of $J_0 = 10$ reveals the coherence between the highest rotational states $J = 17$ and 16, which corresponds to the combination of a third-order polarization induced $\Delta J = 2$ excitation with a hyperpolarizability induced $\Delta J = 1$ excitation. For initial state $J_0 = 16$, the number of the spectrum peaks reduces. This is primarily due to the increasing energy gaps between higher rotational states, which makes the transition to higher states less likely to happen. Overall, the spectra shown in Fig. 6 clearly indicate the enhancements of three-photon Raman transitions by the polarizability-induced alignment excitations.

Our simulations and analysis show that high-order Raman processes are influenced by laser intensity and initial rotational states. Figure 7 demonstrates how a two-color pulse excitation scheme can simultaneously impact molecular alignment and orientation by varying laser intensities and pulse widths, considering both ultracold and room-temperature scenarios. Our simulations indicate that intense short pulses can achieve alignment exceeding 0.9 at ultracold temperatures $T = 0$ K when the initial state is $J_0 = 0$, as shown in Fig. 7(a). Achieving molecular orientation above 0.5 requires high pulse intensity and width matching, as depicted in Fig. 7(b). The overall trends in Figs. 7(a) and 7(b) also unveil an interesting relationship between the transition process and the maximum degree of alignment and orientation. In Fig. 7(a), we observe that the maximum degree of alignment is directly related to both $I_0$ and $\tau_0$ in the lower left region, corresponding to situations where the pulse area is relatively small and lower-order transitions dominate. Increased intensity or longer duration can enhance alignment within this region. However, as intensity and duration increase further, leading to more pronounced multiorder transitions, the $\langle \cos^2 \theta \rangle_{\max}$ begins to decrease due to the destructive interference with higher rotational states resulting from higher-order transitions.
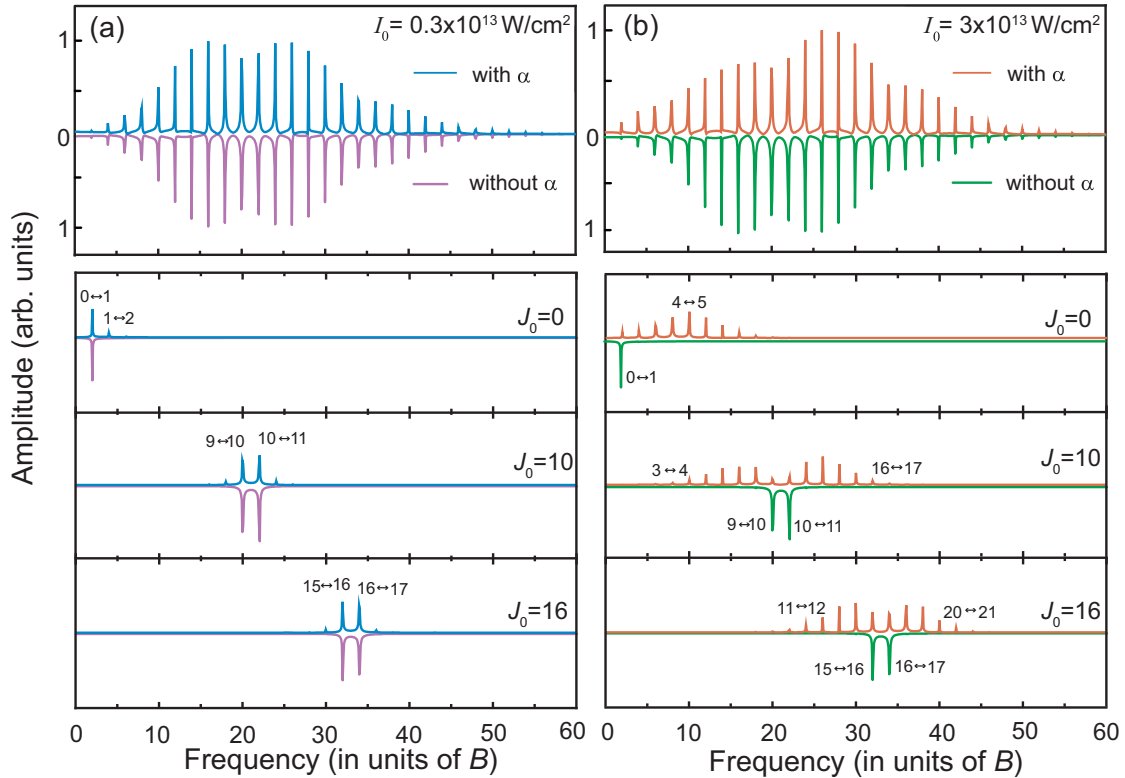
FIG. 6. Fourier transform of the CO molecular orientation signals for (upper row) overall rotational states and (lower row) some of the initial rotational states with the excitation laser intensities of (a) $I_0 = 0.3 \times 10^{13}$ W/cm$^2$ and (b) $I_0 = 3 \times 10^{13}$ W/cm$^2$. The paired spectra correspond to the results calculated with and without considering the polarizability $\alpha$, respectively.
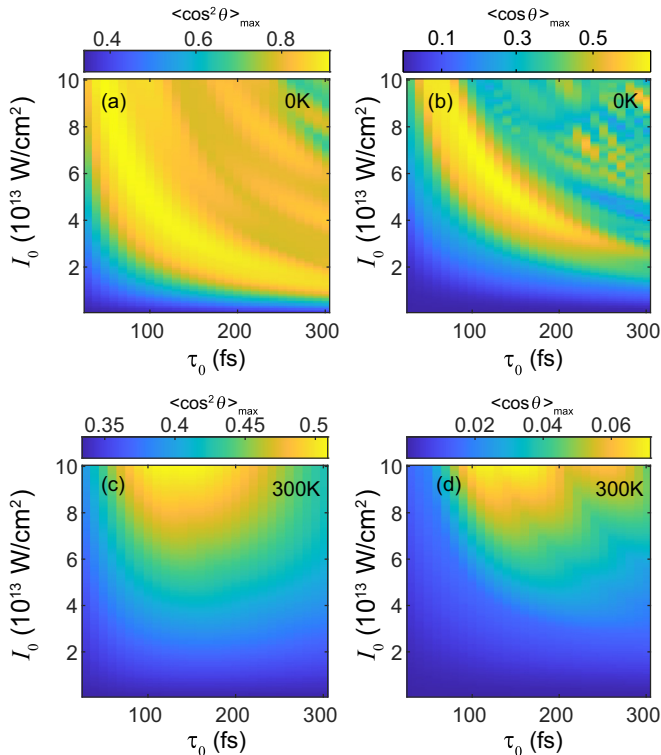


FIG. 7. The dependence of the maximum degrees of the molecular alignment and orientation on the laser intensity and pulse duration at different temperatures. (a) Alignment at 0 K. (b) Orientation at 0 K. (c) Alignment at 300 K. (d) Orientation at 300 K.

The results for room temperature $T = 300$ K are shown in Figs. 7(c) and 7(d). The maximum degrees of alignment and orientation display similarities and differences compared to the results obtained at ultracold temperatures. Overall, we observe that the maximum degrees of alignment and orientation become smaller. This is due to the combination of signals from multiple initial states, reducing the proportional area around the bottom left. In Fig. 7(c), the highest degree of alignment tends to be located in the area with higher intensity and appropriate duration. An alignment degree of 0.5 is achieved for the alignment with $\tau_0 = 130$ fs and $I_0 = 10 \times 10^{13}$ W/cm$^2$. The maximum degree of alignment decreases significantly due to the combination of different initial states. Similar results are observed for the degree of orientation in Fig. 7(d).

It is important to note that in practical experiments, high laser intensities are typically avoided to prevent molecular ionization. Our simulations show that a multiorder Raman transition can enhance molecular alignment and orientation. However, more complex transitions may reduce the degree of alignment and orientation. A multistep transition, i.e., using multiple pulses that induce only a lower-order transition, may efficiently enhance molecular alignment and orientation.

## IV. CONCLUSION

We examined nonresonant Raman transitions in molecular alignment and orientation, considering different laser intensities. Our findings revealed that under low laser intensity, primarily one-order transitions occur, whereas under high laser intensity, multiorder Raman transitions emerge, leading

to enhanced molecular alignment and orientation. We utilized the Dyson expansion of the unitary operator to elucidate the occurrence of multiorder Raman transitions in single-color-laser-induced alignment. Additionally, we delved into the transition process induced by two-color pulses, taking into account the role of polarizability interaction in orientation. Our results confirmed the presence of multiorder Raman transitions in laser-induced alignment and orientation. Finally, we showed how the degrees of alignment and orientation are affected by multiorder Raman transitions as the laser intensity is increased and the pulse duration is varied. These insights significantly contribute to the comprehensive understanding of pulsed laser-induced molecular alignment and orientation through multiorder Raman transitions.

[1] H. Stapelfeldt and T. Seideman, Rev. Mod. Phys. **75**, 543 (2003).

[2] C. P. Koch, M. Lemeshko, and D. Sugny, Rev. Mod. Phys. **91**, 035005 (2019).

[3] Q.-Q. Hong, Z.-Z. Lian, C.-C. Shu, and N. E. Henriksen, Phys. Chem. Chem. Phys. **25**, 32763 (2023).

[4] T. Kanai, S. Minemoto, and H. Sakai, Nature (London) **435**, 470 (2005).

[5] T. Kanai, S. Minemoto, and H. Sakai, Phys. Rev. Lett. **98**, 053002 (2007).

[6] G. Karras, E. Hertz, F. Billard, B. Lavorel, J.-M. Hartmann, O. Faucher, E. Gershnabel, Y. Prior, and I. S. Averbukh, Phys. Rev. Lett. **114**, 153601 (2015).

[7] I. V. Litvinyuk, K. F. Lee, P. W. Dooley, D. M. Rayner, D. M. Villeneuve, and P. B. Corkum, Phys. Rev. Lett. **90**, 233003 (2003).

[8] H. Li, D. Ray, S. De, I. Znakovskaya, W. Cao, G. Laurent, Z. Wang, M. F. Kling, A. T. Le, and C. L. Cocke, Phys. Rev. A **84**, 043429 (2011).

[9] J. L. Hansen, L. Holmegaard, J. H. Nielsen, H. Stapelfeldt, D. Dimitrovski, and L. B. Madsen, J. Phys. B **45**, 015101 (2012).

[10] C. Zhang, J. Yao, F. A. Umran, J. Ni, B. Zeng, G. Li, and D. Lin, Opt. Express **21**, 3259 (2013).

[11] L. Xu, I. Tutunnikov, L. Zhou, K. Lin, J. Qiang, P. Lu, Y. Prior, I. S. Averbukh, and J. Wu, Phys. Rev. A **102**, 043116 (2020).

[12] Z. Lian, Z. Hu, H. Qi, D. Fei, S. Luo, Z. Chen, and C.-C. Shu, Phys. Rev. A **104**, 053105 (2021).

[13] S. Xu, G. Liu, and Y. Huang, J. Phys. B **55**, 155401 (2022).

[14] G. J. Simpson, V. García-López, A. Daniel Boese, J. M. Tour, and L. Grill, Nat. Commun. **10**, 4631 (2019).

[15] E. J. Zak, A. Yachmenev, and J. Küpper, Phys. Rev. Res. **3**, 023188 (2021).

[16] Y. Guo, X. Gong, S. Ma, and C.-C. Shu, Phys. Rev. A **105**, 013102 (2022).

[17] L.-B. Fan, C.-C. Shu, D. Dong, J. He, N. E. Henriksen, and F. Nori, Phys. Rev. Lett. **130**, 043604 (2023).

[18] Z. Lian, Z. Chen, J. Li, C.-C. Shu, and Z. Hu, Phys. Rev. A **108**, 063108 (2023).

[19] J. Itatani, J. Levesque, D. Zeidler, H. Niikura, H. Pépin, J. C. Kieffer, P. B. Corkum, and D. M. Villeneuve, Nature (London) **432**, 867 (2004).

[20] C. Vozzi, M. Negro, F. Calegari, G. Sansone, M. Nisoli, S. De Silvestri, and S. Stagira, Nat. Phys. **7**, 822 (2011).

[21] C. Rose-Petruck, R. Jimenez, T. Guo, A. Cavalleri, C. W. Siders, F. Rksi, J. A. Squier, B. C. Walker, K. R. Wilson, and C. P. Barty, Nature (London) **398**, 310 (1999).

[22] J. Wu, H. Cai, H. Zeng, and A. Couairon, Opt. Lett. **33**, 2593 (2008).

[23] F. Wang, J.-S. Lin, and K. Liu, Science **331**, 900 (2011).

[24] V. V. Albert, J. P. Covey, and J. Preskill, Phys. Rev. X **10**, 031050 (2020).

[25] F. Rosca-Pruna and M. J. J. Vrakking, Phys. Rev. Lett. **87**, 153902 (2001).

[26] M. Leibscher, I. S. Averbukh, and H. Rabitz, Phys. Rev. A **69**, 013402 (2004).

[27] T. Seideman and E. Hamilton, Adv. At. Mol. Opt. Phys. **52**, 289 (2005).

[28] M. Renard, E. Hertz, S. Guérin, H. R. Jauslin, B. Lavorel, and O. Faucher, Phys. Rev. A **72**, 025401 (2005).

[29] P. J. Bustard, R. Lausten, and B. J. Sussman, Phys. Rev. A **86**, 053419 (2012).

[30] S. De, I. Znakovskaya, D. Ray, F. Anis, N. G. Johnson, I. A. Bocharova, M. Magrakvelidze, B. D. Esry, C. L. Cocke, I. V. Litvinyuk, and M. F. Kling, Phys. Rev. Lett. **103**, 153002 (2009).

[31] J. Wu and H. Zeng, Phys. Rev. A **81**, 053401 (2010).

[32] K. Lin, I. Tutunnikov, J. Qiang, J. Ma, Q. Song, Q. Ji, W. Zhang, H. Li, F. Sun, X. Gong *et al.*, Nat. Commun. **9**, 5134 (2018).

[33] S. Wang and N. E. Henriksen, Phys. Rev. A **102**, 063120 (2020).

[34] L. Xu, I. Tutunnikov, Y. Prior, and I. S. Averbukh, J. Phys. B **54**, 164003 (2021).

[35] M. M. Hossain, X. Zhang, S. Minemoto, and H. Sakai, J. Chem. Phys. **156**, 041101 (2022).

[36] B. Friedrich and D. Herschbach, Phys. Rev. Lett. **74**, 4623 (1995).

[37] M. Machholm and N. E. Henriksen, Phys. Rev. Lett. **87**, 193001 (2001).

[38] D. Sugny, A. Keller, O. Atabek, D. Daems, C. M. Dion, S. Guérin, and H. R. Jauslin, Phys. Rev. A **69**, 033402 (2004).

[39] C.-C. Shu, K.-J. Yuan, W.-H. Hu, J. Yang, and S.-L. Cong, Phys. Rev. A **78**, 055401 (2008).

[40] C.-C. Shu, K.-J. Yuan, W.-H. Hu, and S.-L. Cong, J. Chem. Phys. **132**, 244311 (2010).

[41] C.-C. Shu and N. E. Henriksen, Phys. Rev. A **87**, 013408 (2013).

[42] S.-L. Liao, T.-S. Ho, H. Rabitz, and S.-I. Chu, Phys. Rev. A **87**, 013429 (2013).

[43] Q.-Q. Hong, L.-B. Fan, C.-C. Shu, and N. E. Henriksen, Phys. Rev. A **104**, 013108 (2021).

[44] C.-C. Shu, Q.-Q. Hong, Y. Guo, and N. E. Henriksen, Phys. Rev. A **102**, 063124 (2020).

[45] K. Oda, M. Hita, S. Minemoto, and H. Sakai, Phys. Rev. Lett. **104**, 213901 (2010).

[46] C. Chen, J. Wu, and H. Zeng, Phys. Rev. A **82**, 033409 (2010).

[47] X. Ren, V. Makhija, H. Li, M. F. Kling, and V. Kumarappan, Phys. Rev. A **90**, 013419 (2014).

[48] S. Luo, R. Zhu, L. He, W. Hu, X. Li, P. Ma, C. Wang, F. Liu, W. G. Roeterdink, S. Stolte, and D. Ding, Phys. Rev. A **91**, 053408 (2015).

[49] Y. Huang and S. Xu, Eur. Phys. J. D **75**, 181 (2021).

[50] Y. Huang, H. Chen, G. Liu, and S. Xu, Phys. Rev. A **107**, 053108 (2023).

[51] Z. Lian, S. Luo, H. Qi, Z. Chen, C.-C. Shu, and Z. Hu, Opt. Lett. **48**, 411 (2023).

[52] A. Mitra and H. Rabitz, Phys. Rev. A **67**, 033407 (2003).

[53] A. Mitra, I. R. Solá, and H. Rabitz, Phys. Rev. A **67**, 043409 (2003).

[54] Y. Huang, G. Liu, and S. Xu, Chin. Opt. Lett. **20**, 100005 (2022).